The Inter-Bristle Pressure Filed in a Large-Scale Brush Seal

Joshua P Bowen[1], Matthew R Jenkins[2], Aaron A Bowsher[2], Peter F Crudgington[2], Carl M Sangan[1], and James A Scobie[1]
jpb50@bath.ac.uk, matthew.jenkins@crossmanufacturing.com, aaron.bowsher@crossmanufacturing.com, pete.crudgington@crossmanufacturing.com, c.m.sangan@bath.ac.uk, and j.a.scobie@bath.ac.uk
[1]Department of Mechanical Engineering
University of Bath
Bath, BA2 7AY
United Kingdom
[2]Cross Manufacturing Co. (1938) Ltd.
Devizes
United Kingdom

ABSTRACT

Brush seals promise improvements to the widely used labyrinth seal in regulating turbomachinery leakages. Enhanced resistance to the flow is provided by a static ring of densely packed fine wire bristles that are angled in the direction of rotation and flex to accommodate rotor excursions. A large-scale brush seal was constructed to study the leakage characteristics in *direct relation* to the pressure field within and surrounding the bristle pack for multiple clearance conditions, therefore developing the understanding of brush seal fluid dynamic behaviour.

The governing parameter controlling leakage behaviour transitioned from pressure ratio for a large clearance, to pressure load for a line-on-line configuration. In all cases, leakage flow converged to an asymptotic value once maximum levels of bristle blow-down and pack compaction were attained. For both clearance configurations, this occurred at a pressure ratio corresponding to that at which axial distributions of pressure converged; equivalent behaviour was noted for the line-on-line configuration with pressure drop. Comparatively small changes were experienced in leakage behaviour

and to the inter-bristle pressure field with increasing pressure drop for the line-on-line brush seal. This indicated that brush seal performance is more influenced by changes in bristle blow-down than bristle pack compaction.

1 INTRODUCTION

The gas turbine is employed across a range of applications, including aviation and power generation; the large energy density, range of power outputs and fuel versatility offer significant advantages over alternative technologies. With environmental legislation demanding ever greater fuel efficiency, more effective use of the secondary air system (SAS) is critical. The SAS delivers bleed air, diverted from the main gas path in the compressor, to cool life-limited turbine hardware and to seal bearing and disc cavities. A performance penalty is incurred as a result of the SAS bypassing the combustor and turbine annulus; work expended in compressing the air prior to its bleed point is also a parasitic loss. A recent study suggests that a 1% reduction in engine bleed correlates to an annual worldwide saving of 280 million gallons of airline fuel [1].

Seals are used to regulate leakages in turbomachinery by controlling interface clearances. The seals located between rotating and stationary components have been identified as the most cost-effective method of enhancing gas turbine performance [1] [2]. Approximately 50 leakage pathways critical to overall performance are present in a typical turbine [2], throughout which seals must operate with extreme reliability and predictable in-service performance, whilst often being subjected to intense thermal and centrifugal loads.

Labyrinth seals consist of a series of teeth that form aperture cavities through which flow energy is dissipated [1]. These are commonplace in gas turbines due to their proven reliability and represent a low cost, long life sealing arrangement with a wide

range of application [2]. Performance is dependent on the radial clearance between the teeth tips and opposing surface, which must be sufficiently large to prevent rotor-stator contact during rotor excursions and thermal growth. Therefore, seal performance must often be sacrificed to protect hardware.

Brush seals provide resistance to flow using a bristle pack, which is made up of closely packed flexible fine wire bristles that protrude radially inwards at a lay angle. The brush seal can be installed with a build clearance, as illustrated in the cross-sections shown in Fig.1, or in interference, whereby the bristles are displaced by the rotor. The bristle pack is typically clamped and welded between a front plate on the high-pressure side, providing protection from the incoming flow and during installation [3], and a back plate on the low-pressure side, which structurally supports the bristles to allow operation at high pressure loads.

The bristles are canted and hence contact-compliant, being able to bend to accommodate rotor excursions without buckling [1] [4]; ergo permanent wear and degradation of sealing performance are avoided, unlike with labyrinth seals. Tighter clearances can readily be achieved, corresponding to significant performance gains. Leakage flow rates can be 5-10% of those from similar labyrinth seals [5]. Improvements of this magnitude in sealing efficiency has been found to translate to a 3% rise in engine thrust [4] and a 5% reduction in specific fuel consumption [6]. These performance gains are maintained even as the bristles wear; the bristles move radially inwards to close the clearance under a pressure load in a process known as blow-down [7]. Furthermore, brush seals occupy significantly less axial space than labyrinth seals [1], presenting practicality benefits for ease of assembly and maintenance [4], and do not promote rotordynamic instabilities [2].

Despite obvious performance gains, the use of brush seals is principally limited by a high seal stiffness [8] and an incomplete understanding of their fluid dynamic behaviour. This paper presents experimental measurements from a large-scale brush seal (LBS) of ten-times scale and is the first study to robustly characterise the leakage flow through brush seals in *direct relation* to the inter-bristle pressure field. These parameters are studied comprehensively for three clearance conditions and over a wide range of pressure loads to provide an enhanced aerodynamic understanding that is of importance to future brush seal application and analysis.

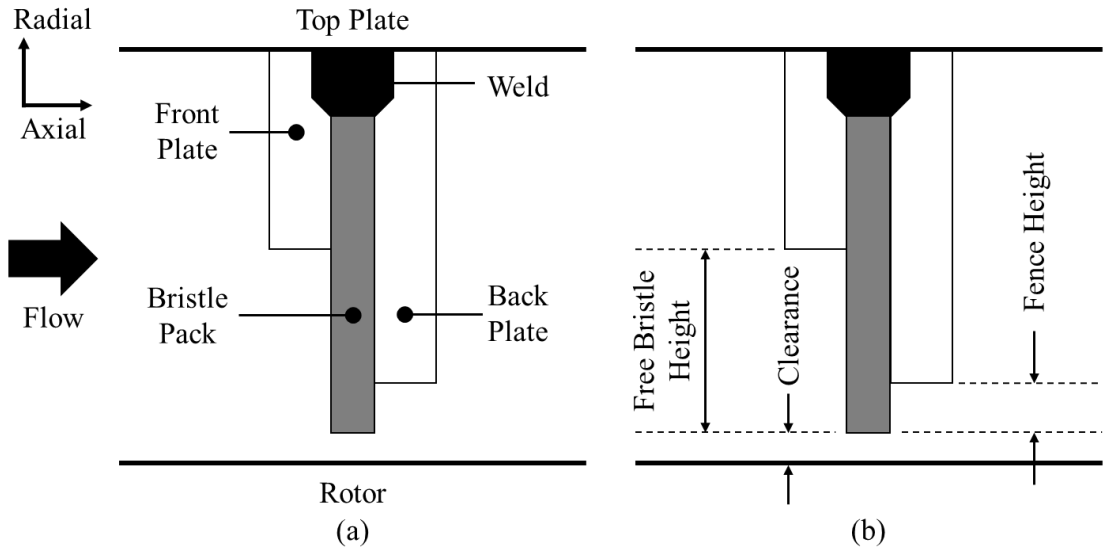

Figure 1: Schematic cross-section of a brush seal, annotated to show: (a) key features; (b) salient dimensions.

2 LITERATURE REVIEW

This section presents a brief review of research concerning brush seals, including investigations focussing on both experimental and computational analysis. Where appropriate, post-analysis of published data has been performed to aid comparison with the results presented in Section 5. To ensure consistency when analysing data from

different studies, results have been re-plotted using standardised axes and nomenclature, as described in Section 3.4.

A comprehensive overview of sealing in turbomachinery, including both brush and labyrinth seals, is provided by Chupp *et al.* [1]. For an extensive review of published literature see Aslan-Zada *et al.* [2], who detail the application of brush seals in gas turbines as an alternative to labyrinth seals. The authors conclude that brush seals demonstrate the ability to reduce both gas turbine fuel consumption and overall emissions, but acknowledge the need for further study, highlighting a lack of experimental testing in realistic engine operating environments. The benefits arise from the ability of brush seals to substantially reduce leakage flow rates in comparison to

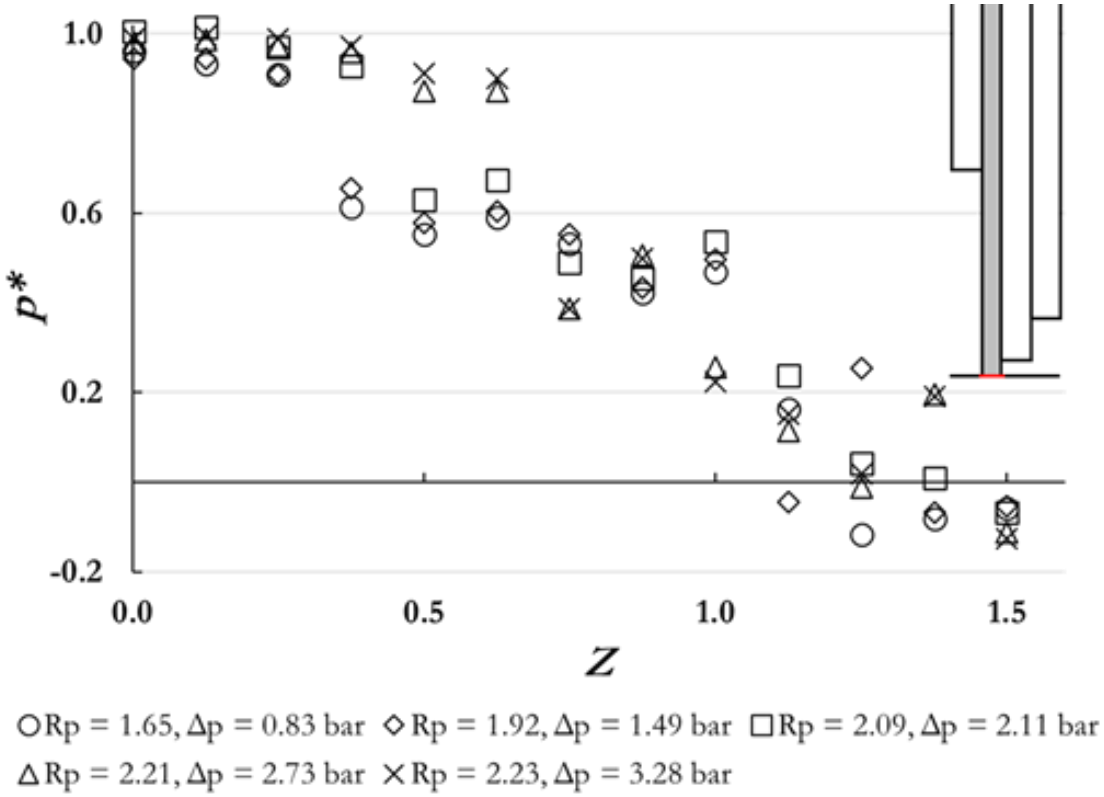

Figure 2: Measured distributions of axial pressure along the rotor surface (highlighted) of an interference seal for different pressure ratios; adapted from Chen [13].

labyrinth seals, a conclusion reported consistently across various studies [1] [2] [4] [6] [9] [10].

Dinc *et al.* [3] and Kirk *et al.* [11] provide an insight into the brush seal design process, explaining the significance of poor design, integration, and key seal dimensions on hardware service life, seal performance and wear rate. Again, the importance of understanding brush seal behaviour is acknowledged [3], with analysis carried out to conclude that there is a need to compromise on seal characteristics when accounting for allowable stress limitations.

Two of the most thorough experimental analyses of the fluid dynamic behaviour of brush seals were performed by Bayley & Long [12], and Chen *et al.* [13] [14], who both compare their experimental data with predictions made by porous medium models. Bayley & Long [12] measured axial and radial pressure distributions along the rotor and back plate surfaces respectively, using a circular - but non-rotating - brush seal test rig, built with an interference of 0.25 mm. Chen *et al.* [13] [14] gathered experimental data using a five-times scale brush seal in a cascade configuration that allowed for static pressure measurements to be made throughout the bristle pack, as well as on the rotor and back-plate surfaces. The seal was tested with a clearance and an interference fit. This study was the first to embed hollow tubes in place of replica bristles within the pack to measure static pressure in the inter-bristle field.

The pressure drop across a brush seal has been shown to be near-linear through the bristle pack with axial position [12] [14], with further agreement provided by Braun *et al.* [15]. The exception to this was found by Chen *et al.* [13] [14], who showed a non-linear two-gradient trend; the axial pressure drop forming during smaller pressure differentials was attributed to the compaction of the upstream bristles creating the first

region of high flow resistance, and the flow area contraction underneath the back plate creating the second. Both regimes can be seen in Fig. 2. Tests at higher pressure ratios also resulted in greater relative pressure being maintained further into the bristle pack, indicated by greater p* values at higher pressure ratios for $0.4 < Z < 0.6$ in Fig. 2.

Results by Bayley & Long [12] and Chen *et al.* [13] [14] also exhibit a substantially varying porosity in the bristle pack, derived through comparison of their computational and experimental results. This was attributed to the bristle deflections under loading and the resulting pack compaction, which is particularly prominent in the fence height region. The model constructed by Doğu [16] accounted for this variation.

Studies by Bayley & Long [12] and Chen *et al.* [13] [14] provide insight into the nature of the pressure drop across a brush seal but only test over a limited range of operating conditions; furthermore, both only investigate brush seals with shallow front plate designs that have poor geometric similitude to operational seals and present data with significant scatter over a wide range of pressure loadings. Therefore, the accuracy and geometrical relevance of the empirical data for calibration of porous medium model must be improved.

Chen *et al.* [14] also study the leakage characteristics of a large-scale brush seal in clearance and interference configurations to prove its similarity with a rotating brush seal. Further analysis in this field was performed by Crudgington [17], who concludes that the leakage performance is characterised by the pressure drop across the seal but does not investigate the effect of pressure ratio for clearance seals. Crudgington [17] also highlights the importance of bristle diameter and fence height to seal leakage, characterised in terms of effective clearance. Finally, Pekris *et al.* [8] analyse the impact of back plate configuration on effective clearance. Despite much work investigating the

leakage characteristics in brush seals, the value in comprehensively studying the leakage characteristics over a wide range of pressure loads and clearances is paramount.

3 EXPERIMENTAL FACILITY

3.1 Large-Scale Brush Seal (LBS)

Brush seals employed in gas turbines are typically small, with bristle diameters and lengths around 70 μm and 15 mm respectively [14]; in the engine they are subjected to high-speed rotational motion. Investigating the flow behaviour at this scale and under these conditions is extremely difficult. The LBS experimental rig at the University of Bath consists of a large-scale brush seal in a cascade configuration to overcome these challenges whilst maintaining representative seal behaviour. A typical aero engine design was adapted so that the bristle diameter and bristle pack stiffness were scaled by a factor of ten using a proven design tool. Correct inter-bristle behaviour was ensured through appropriate material selection and processed with electro-discharge machining, so that a similar coefficient of friction at room temperature was obtained. Data published by Crudgington et al. [18] shows near identical pack stiffness, bristle tip pressure, and packing density between a studied brush seal of typical design and the LBS, when values were normalised by bristle diameter. Therefore, the LBS is geometrically and physically similar to a typical operational brush seal.

A maximum working pressure of 7.5 bar (gauge) allowed for a variety of different working pressure loads and ratios to be applied across the seal. The test rig consists of three key modules, as shown in Fig. 3. Full technical data is shown in Table 1, including the geometric values for the three clearance configurations reported in this study.

The test section encloses the seal within a pressure combatant housing and consists of the bristle pack assembly, front and back plates, and outer casings (which direct the

flow towards the seal and join the assembly with the rig housing). During design of this linear seal, considerations were made to

ensure correct bristle deflection throughout and to mitigate against the influence of seal end effects on the leakage flow. The bristle pack is made up of 3,336 stainless steel 304 hypodermic tubes that are tightly bundled together in 12 rows and assembled at a lay angle of 45°; a photograph of the brush seal can be seen in Fig. 4. Each tube represents a single bristle and is of 1.02 mm diameter. Due to the modular design of the LBS, the front and back plates can be readily replaced in order to integrate different geometries. The position of the seal within the test section is adjustable, allowing for various clearances to be tested. A detachable aluminium 7075 plate acts as the equivalent rotor surface positioned underneath the seal clearance. The rotor plate includes static pressure ports, flush-mounted to the surface; the rotor plate can be interchanged with a reinforced glass window that allows for optical access.

Four aluminium 7075 chambers make up the remainder of the LBS rig, which are constructed in a parallelogram-based prism shape to simulate the annular flow space inside a gas turbine and account for the bristle lay angle. Three upstream chambers separated by flow straighteners promote the development of the flow before entry to the test section.

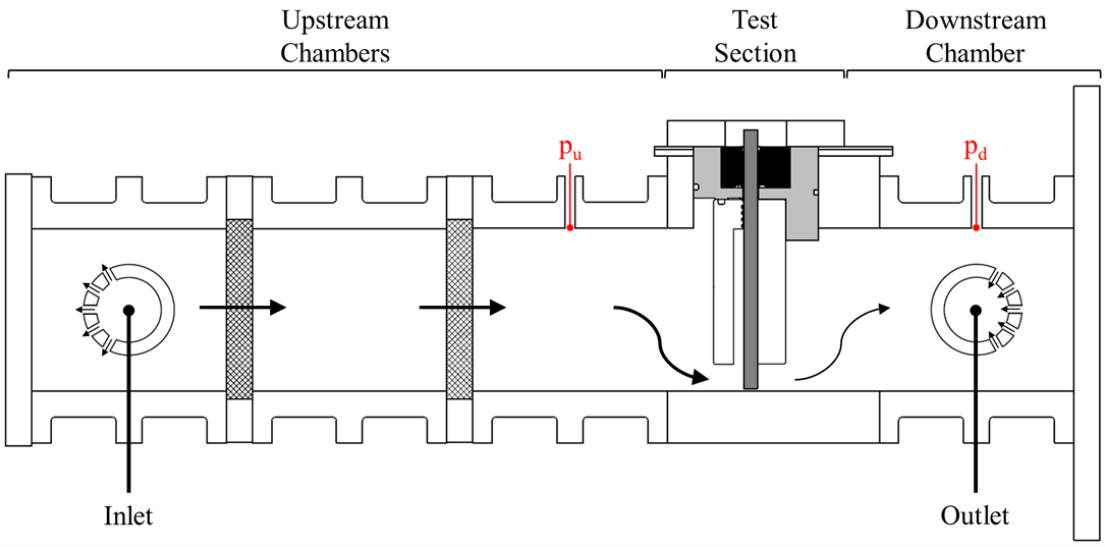

Figure 3: Cross-section view of the LBS test rig, highlighting the three key modules, flow path, and upstream (p_u) and downstream (p_d) static pressure measurement locations.

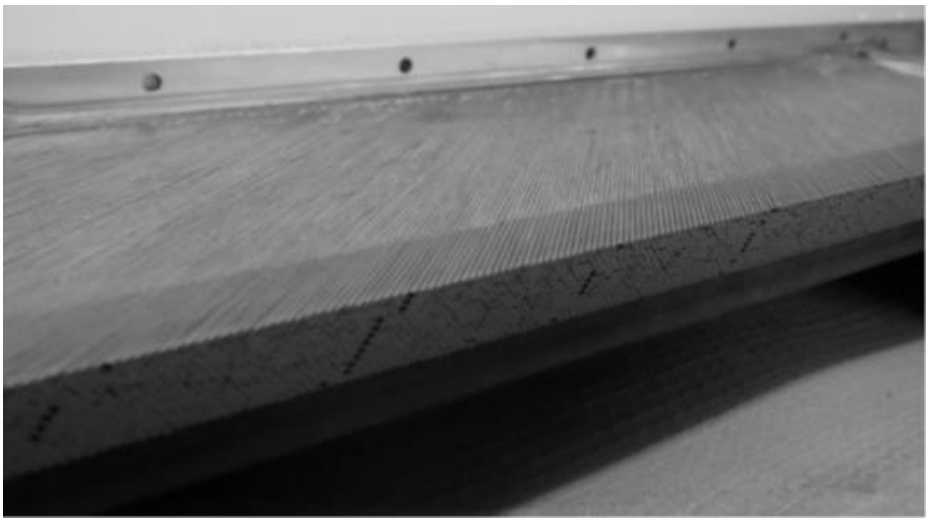

Figure 4: The LBS with the front plate removed to expose the canted bristle pack. The hollow bristle tip locations can be identified.

Table 1: Technical data of the LBS experimental rig.

Parameter	Value (Metric)	Value (Imperial)
h_{fb}	123.20 mm	4.85 in.
h_f	19.06 mm	0.75 in.
t_{bp}	10.77 mm	0.42 in.
z_{fb}	18.47 mm	0.73 in.
D	1.02 mm	0.04 in.
φ	45°	45°
c_m	0, 0.98, 1.95 mm	0, 0.04, 0.07 in.
c	0, 1.0, 1.9	0, 1.0, 1.9
ρ	10.61 kg/m^3	0.66 lb/ft^3
E	193 GPa	28,000 ksi
No. of bristle rows	12	12
Packing density	8.50/mm	216/inch
Test section length	163.25 mm	6.43 in.
Test section height	125.39 mm	4.94 in.
Test section depth	358.14 mm	14.10 in.

3.2 Instrumentation

Static pressure measurements were acquired throughout the LBS, with the aim of interrogating the flow field in greater detail than previously possible. Figures 3 and 5 illustrate the measurement locations within the bristle pack, at the back plate, on the rotor surface, and in both upstream and downstream chambers; all are located in the

centre of the test section to minimise any end effects. Static pressure was recorded in the bristle pack for all 12 rows at the four spanwise heights indicated in Fig. 5 and Table 2, with measurements on the back plate surface being made at consistent locations to H2, H3 and H4. The static pressure measurement locations on the rotor surface were designated R1 to R14 and assigned the spanwise location H0.

Hollow stainless steel 304 tubes embedded within the bristle pack allowed for static pressure readings in this region. Some of the tubes were sealed with Inconel 718 wire bungs and contained a 0.51 mm hole in the tube wall to collect data at specified spanwise height rather than at the bristle tips. Validation of this method is provided by Chen et al. [14]. Hollow stainless steel 304 tubes are also inserted into counter-bored holes drilled into the back plate and the detachable aluminium rotor plate for analysis of the flow field around the bristle pack. Finally, compression fittings allowed for the placement of further pressure taps in the upstream and downstream chamber walls, so that the pressure boundary conditions either side of the brush seal could be determined.

The static pressure measurements, made at the location of the opening of each stainless steel 304 hollow tube, were determined using HMA Series Amplified Pressure Sensors, utilising a National Instruments CompactDAQ data acquisition system and LabVIEW analysis software. Each static pressure datapoint documented hereafter represents the mean value over a stable 20 second period, eliminating the effect of noise.

Compressed air supplied to the LBS rig was controlled via a manual ball valve and an electronic Cynergy3 solenoid valve, so that the exact position of the ball valve could be maintained for continuity between different tests. A Bronkhorst F-106CI mass flow meter measured the flow rate up to 0.351 kg/s, for which the data was analysed using LabVIEW software via the CompactDAQ system. A manual Norgren R41 pressure

regulator allowed for the maximum upstream pressure in the LBS to be limited. The temperature was collected downstream of the manual ball valve, mass flow meter and pressure regulator in the inlet pipe.

The optical access provided by the reinforced glass window plate allowed for video analysis of the bristle pack during testing, through which the axial deflection was determined. This methodology is detailed in Appendix A.

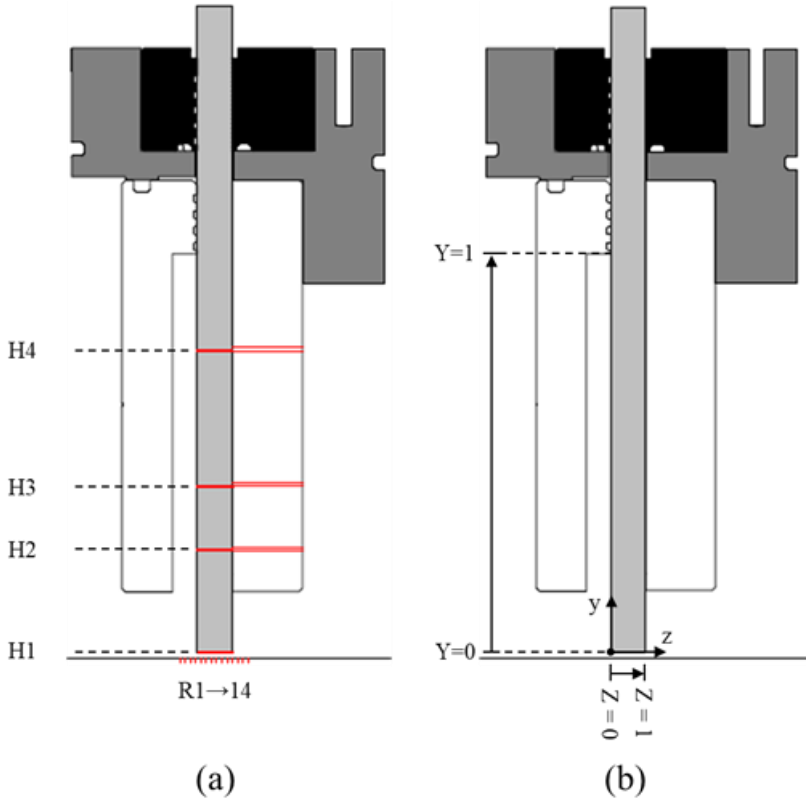

Figure 5: Cross-section views of the test section: (a) highlighting the static pressure measurement locations; (b) defining the dimensionless axes.

Table 2: Normalised static pressure measurement locations in the test section of the LBS.

	Tap	*Y*	*Z*
Spanwise Distribution	*H1*	0.00	-
	H2	0.26	-
	H3	0.42	-
	H4	0.76	-
Axial Distribution	*R1*	-	-0.50
	R2	-	-0.35
	R3	-	-0.20
	R4	-	-0.05
	R5	-	0.10
	R6	-	0.25
	R7	-	0.40
	R8	-	0.55
	R9	-	0.70
	R10	-	0.85
	R11	-	1.00
	R12	-	1.15
	R13	-	1.30
	R14	-	1.45

3.3 Operating Conditions

The LBS was tested at two spanwise clearances, c_m, of 0.98 mm and 1.95 mm, in addition to a line-on-line (LoL) case where c_m = 0. These clearances were normalised based on the bristle diameter and so were represented by c = 1.0, 1.9 and 0 (LoL), respectively.

All three clearances were tested with an atmospheric p_d, where the outlet valve was fully opened. In these cases, $\dot{m}$ was steadily increased, leading to a rise in p_u, R_p and Δp; a small drop in p_d was also experienced with increasing $\dot{m}$.

For c = 1.0 and the line-on-line case, further data sets were collected using a fixed p_u utilising the pressure regulator. Starting with an atmospheric p_d, the outlet valve was steadily closed to reduce $\dot{m}$, R_p and Δp.

Due to the large spanwise clearance when c = 1.9, maintaining a constant pu was not possible. To aid comparison with other configurations, two additional data sets were collected for the large clearance case where ṁ remained constant by fixing the position of the inlet ball valve. The outlet valve was steadily closed to increase p_d, leading to a reduction in $\dot{m}$, R_p and Δp. As p_u was not regulated, this also increased as the outlet valve was closed, but at a slower rate than p_d.

The operating conditions for each experiment are summarised in Table 3; these test conditions apply to the data presented in Section 4.

3.4 Non-Dimensional Variables

Presenting results using normalised, dimensionless terms on a standardised axis system allows for consistency when analysing data from different studies and different test conditions. These are defined in Eqs 3.1-3.5 with the normalised axes given in Fig.

5, whereby the origin lies at the front tip of the unloaded bristle pack, with y and z describing

the spanwise and axial locations, respectively. The normalised spanwise location Y = 1 describes the free bristle height, while the normalised axial location Z = 1 locates the back plate front edge. p^* represents the normalised static pressure and Φ the normalised leakage flow rate, known as the flow function. Finally, the effective clearance, c_{eff}, represents the clearance of an annular restriction of the same diameter as the tested seal required to pass the measured leakage isentropically [19] and hence also indicates the seal performance.

$$\boldsymbol{Y = \frac{y}{h_{fb}}} \quad \textbf{(3.1)}$$

$$\boldsymbol{Z = \frac{z}{t_{bp}}} \quad \textbf{(3.2)}$$

$$\boldsymbol{p^* = \frac{p - p_d}{p_u - p_d}} \quad \textbf{(3.3)}$$

$$\boldsymbol{\Phi = \frac{\dot{m}\sqrt{RT}}{p_u L^2}} \quad \textbf{(3.4)}$$

$$\boldsymbol{c_{eff} = \frac{\dot{m}\sqrt{T}}{w p_u Q}} \quad \textbf{(3.5)}$$

4 LEAKAGE CHARACTERISTICS

The leakage performance of the LBS was interrogated for the three clearances; experiments were conducted over a range of operating conditions, as described in Table 3. In each instance, Φ was calculated using Eq. 3.4, with measured values of $\dot{m}$, T and p_u. The relationship between Φ and R_p is shown in Fig. 6; the relationship between Φ and Δp is illustrated in Fig. 7.

In both cases, Φ increases with increasing pressure differential, following an inverse exponential trend and tending to an asymptotic value once maximum bristle blow-down

and pack compaction was achieved. Similar behaviour was found by Chen *et al.* [14] for both clearance and interference configurations. As expected, with reducing clearance, the asymptotic value of Φ decreases in accordance with enhanced resistance to the flow.

It can be noted that at the largest clearance (c = 1.9), data for all three operating conditions demonstrate similar Φ values for a given R_p. However, when plotted against Δp in Fig. 7 the Φ values for c = 1.9 exhibit clear independency with respect to operating condition. This behaviour is reversed when examining the leakage characteristics for the LoL condition, for which the data sets coalesce more closely when Φ is plotted against Δp. Data for the intermediate clearance, c = 1.0, exhibit behaviour more aligned to that shown with the larger clearance, whereby there is increased independence with respect to operating condition when considering the Φ against Δp relationship. Overall, it can be concluded that as the seal clearance is reduced, the leakage behaviour of the LBS progressively transitions from being principally governed by R_p to ultimately being determined by Δp in the LoL case. This is true in this study because the pressure load limit, which states the maximum Δp that the seal can be subjected to before plastic deformation of the bristles, is not exceeded. The conclusions drawn by Crudgington [17] were limited by the small range of variable tested; the greater range of clearances and pressure loads documented in this study provide additional insight.

The dependency on Δp is expected for the LoL condition, for which the only flow path is directly through the porous medium of the bristle pack and subsequently down the face of the back plate in the spanwise direction, as described by Doğu [16]. The compaction of the pack, and hence the porosity of the porous medium, is governed by

the net force it is subjected to. Therefore, Δp can be expected to influence the leakage flow through the LBS in the LoL condition more significantly than R_p.

Doğu *et al.* [20] show that, for an annular brush seal with a radial clearance, the vast majority of the flow does not permeate through the bristle pack but discharges through the clearance region. Therefore, with the large clearance (c = 1.9), the LBS acts similarly to an annular seal in resisting the flow, for which discharge rate is dependent on R_p. When the clearance area is reduced for the c = 1.0 case, a greater proportion of the leakage permeates through the porous bristle pack, but the overwhelming majority still discharges through the clearance.

Figure 8 shows the variation of ceff with R_p for the LBS, which indicates that the effective clearance of the brush seal decreases initially as R_p is raised beyond unity, before reaching a minimum and then gradually increasing with a further rise in R_p. When $R_p \approx 1$, the pressure loading on the bristle pack is very small and hence there is minimal blow-down or compaction, resulting in a maximum clearance area and bristle pack porosity.

For the c = 1.0 and c = 1.9 clearance cases, c_{eff} reduces to approximately 0.87 mm and 1.45 mm respectively, confirming that $c_m > c_{eff}$ for the LBS. This reinforces the sealing benefits provided by a brush seal, where a tighter clearance would be required by an annular restriction of similar arrangement to pass the measured leakage isentropically. Meanwhile, ceff reduces to 0.5 mm for the LoL case, approximately half the diameter of the bristles in the LBS; consistent with findings by Crudgington [17] and with ratios frequently derived by engineers at Cross Manufacturing Co. (1938) Ltd. for operational brush seals, reinforcing the representative behaviour of the LBS.

Similar to the discussion above, the c_{eff} vs. R_p relationships demonstrate behaviour that emphasises the governing parameters for the LBS at different clearance conditions.

Table 3: Operating conditions for the LBS.

c	Test	Inlet Condition	Outlet Condition
1.9	●	Varied	ATM
	△	$\dot{m}$ = 0.19 ± 0.01 kg/s	Varied
	×	$\dot{m}$ = 0.34 ± 0.01 kg/s	Varied
1.0	●	Varied	ATM
	△	p_u = 3.04 ± 0.04 bar	Varied
	×	p_u = 5.52 ± 0.06 bar	Varied
LoL	●	Varied	ATM
	△	p_u = 3.13 ± 0.02 bar	Varied
	×	p_u = 4.56 ± 0.04 bar	Varied

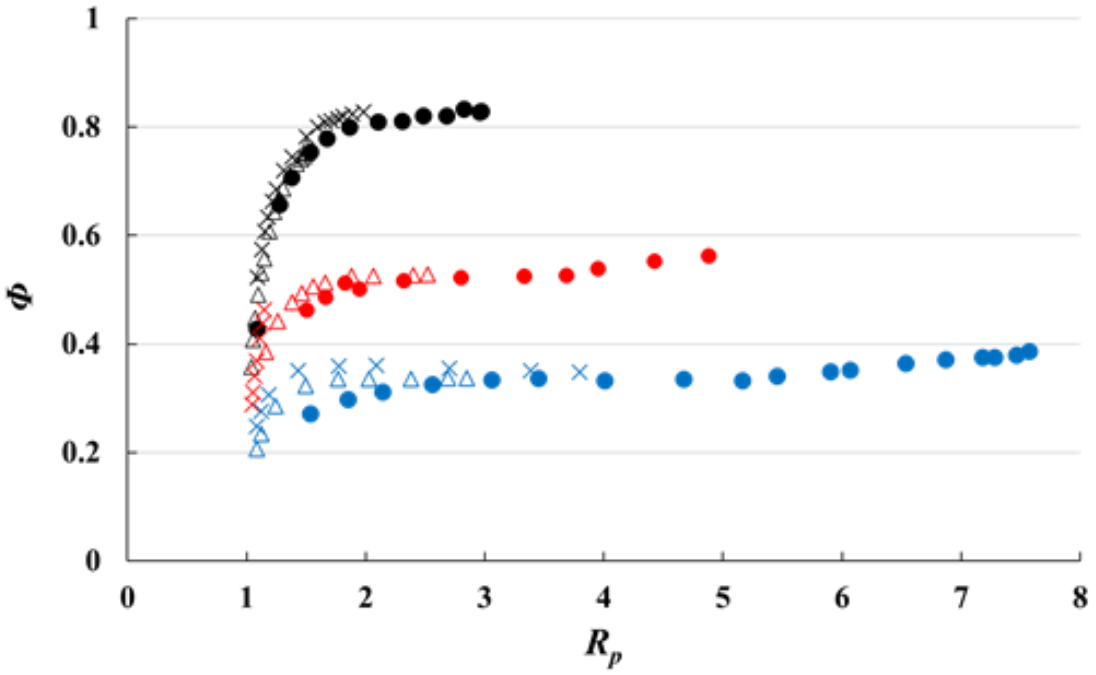

Figure 6: Distribution of Φ with R_p for three clearances across a variety of operating conditions as describes in Table 3.

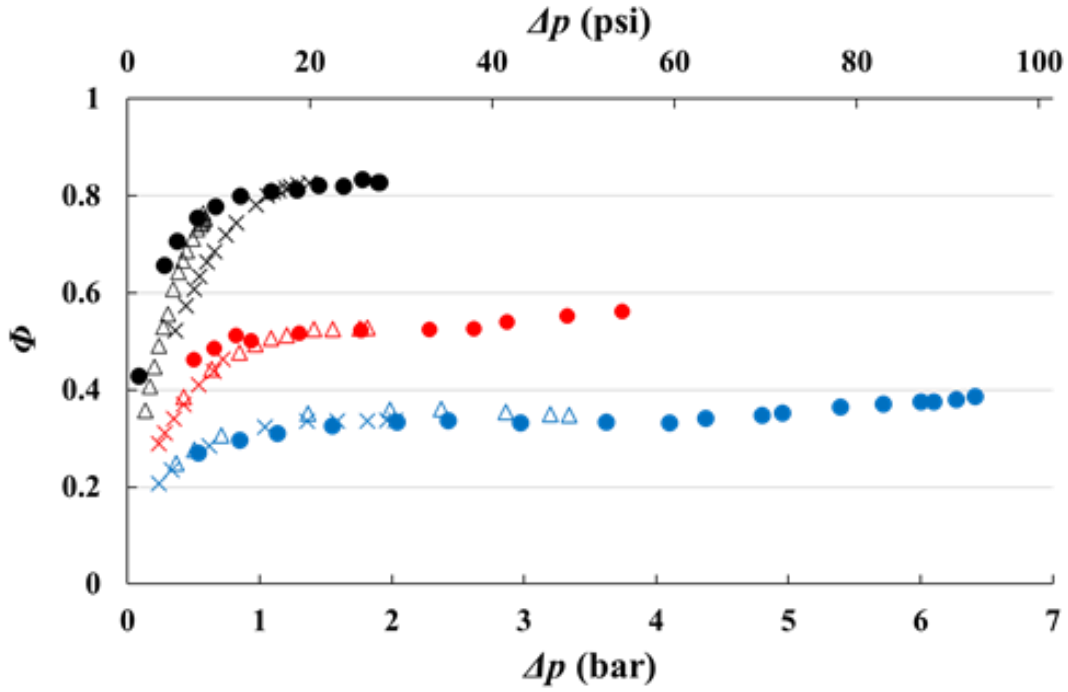

Figure 7: Distribution of Φ with Δp for three clearances across a variety of operating conditions as described in Table 3.

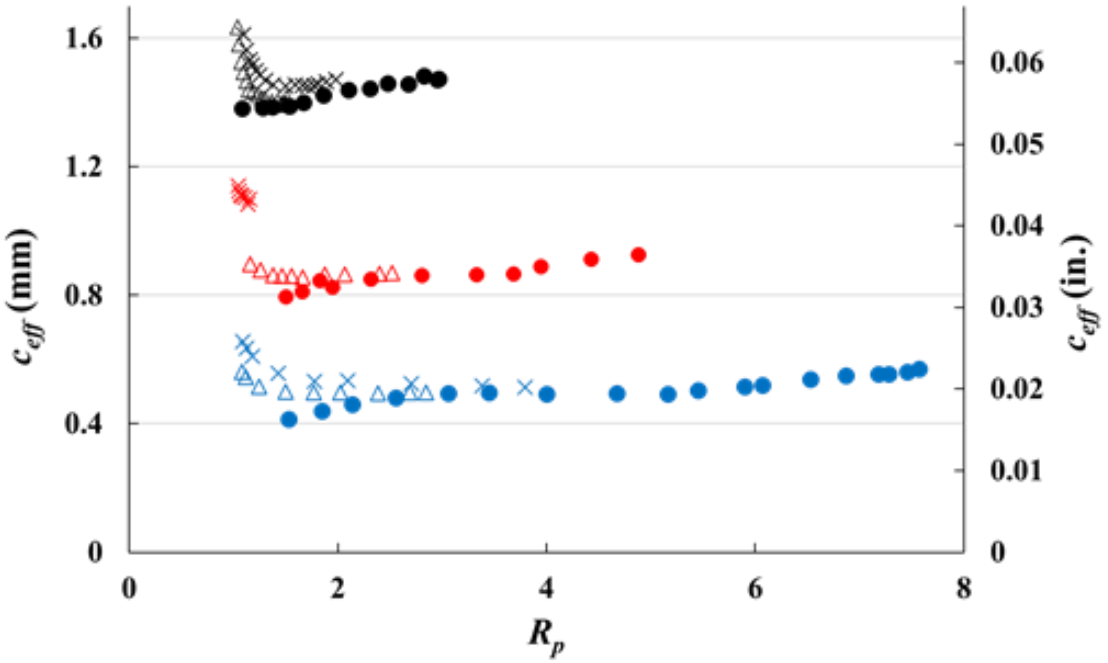

Figure 8: Distribution of c_{eff} with R_p for three clearances across a variety of operating conditions as described in Table 3.

5 INTER-BRISTLE PRESSURE FIELD

In this section, the pressure distribution through the LBS is explored, utilising the measurement locations within the bristle pack, on the rotor surface, and on the back plate. Data for the three clearance conditions are presented in sequential sub-sections, including distributions of pressure on the rotor surface and at the bristle tips (*H0* and *H1* respectively). Data acquired at the bristle tips (*H1*) account for the axial deflection of the bristles under pressure loading; displacements were monitored through video analysis of the bristle tips, with *Z* positions shifted accordingly. An overview of the axial deflection measurements can be found in Appendix A. Finally, the axial pressure drop through the LBS is compared for similar operating conditions at locations *H0*, *H1* and *H4* for the three clearance conditions.

5.1 Large Clearance Condition, c = 1.9

The axial distribution of pressure within the test section of the LBS was studied for six operating conditions for c = 1.9, detailed in Table 4. Results are shown for positions *H0* and *H1* in Fig. 9 and Fig. 10, respectively. Examination of the distributions of pressure for c = 1.9 across the operating conditions presented in Section 4 indicated that p^* through the bristle pack was principally governed by R_p, as was the case for Φ. Therefore, all data presented in this section is for an atmospheric downstream boundary condition, where p_d = ATM, to study the effect of changing pressure ratio.

The pressure drop at *H0* (Fig. 9) can be described in two general stages; a sharp drop in p^* over a short axial distance at the front of the bristle pack, followed by a gradual reduction to $p^* \approx 0$ at Z = 1.45. The change in p^* for each of these two stages is dependent on the pressure ratio, with the extent of the first pressure drop being greater at lower R_p, and the gradient of the second being steeper at higher R_p.

As the incoming flow impacts the brush seal, the load exerted on the first rows is substantial, causing a relatively large bristle deflection. This results in extensive compaction and blow-down at the front of the bristle pack, which provides high resistance to the flow and hence a considerable drop in p^* on the rotor surface. For larger R_p values, a higher p^* was maintained deeper into the bristle pack as a result of increased compaction and blow-down at latter bristle rows, as observed in previous studies [13] [14]. For small R_p values, the pressure downstream of the early bristle rows was insufficient to cause significant pack compaction and blow-down, and so the relative pressure drop across the latter bristle rows in this case was less severe.

The effect of increasing R_p can be seen in Fig. 9 and Fig. 10, whereby the magnitude of p^* and the form of the pressure-drop ultimately converges towards an upper limit.

At both *H0* and *H1*, similar p^* values are apparent at consistent Z positions for $R_p > 3.0$, which corresponds to Φ approaching an asymptote, shown in Fig. 6 for $c = 1.9$.

Figure 9 shows that the location of the initial pressure drop on the rotor surface moves further downstream for larger pressure ratios; for $R_p = 1.5$, a significant drop in p^* occurs between $-0.05 < Z < 0.10$, while for $R_p = 6.4$, this is delayed until $0.10 < Z < 0.25$. This shift is due to the axial displacement of the bristle pack, which deflects further downstream when subjected to larger pressure loads. The impact of bristle deflection is also seen at the rear of the pack; the gradual reduction in p^* observed in the second pressure drop stage continues beyond $Z > 1$ for larger R_p values. The latter rows of the bristle pack deflect around the back plate and continue to provide resistance to the flow. The shifting of the symbols in the Z-direction with increasing pressure ratio in Fig. 10 also indicates the axial deflection of the bristle tips, which is determined from Appendix A.

The change in pressure with axial distance at *H1* (Fig. 10) for large R_p is near-linear for $Z > 0.4$. At smaller R_p values, this trend is less apparent. The axial increase in p^* for $Z < 0.4$ (i.e., until the fourth bristle row) represents a departure from the near-linear decrease in p^* occurring thereafter. This trend was exhibited in all tests reported here across a range of R_p for $c = 1.9$. The positive pressure gradient lessens with increasing R_p (and hence bristle deflection), ergo the magnitude and strength of this low-pressure region is influenced by the displacement of the bristle pack.

Overall, the data presented here shows very little scatter and hence trends can easily be noted. The spatial resolution and fidelity of the data shown here greatly surpasses that published by Bayley & Long [12] and Chen et al. [13][14], which both experience increased scatter at significantly lower pressure loads.

Table 4: Operating conditions for each data set at the c = 1.9 clearance condition. For all cases, p_d = ATM.

Test	Δp (bar)	p_u (bar)	R_p
○	0.5	1.5	1.5
◇	1.3	2.3	2.3
△	2.3	3.3	3.5
×	3.2	4.2	4.5
□	4.1	5.1	5.5
●	4.9	5.8	6.4

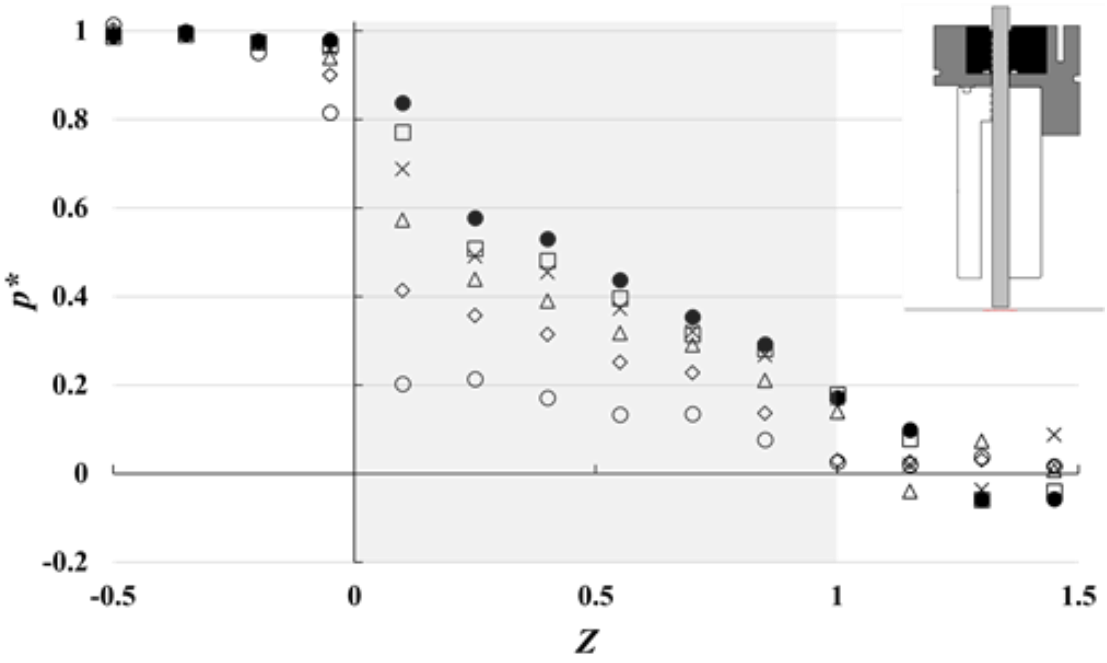

Figure 9: Axial distribution of pressure on the rotor surface, H0, (highlighted) for c = 1.9 and over the range of operating conditions described in Table 4. The unloaded bristle pack location is indicated by the shaded region.

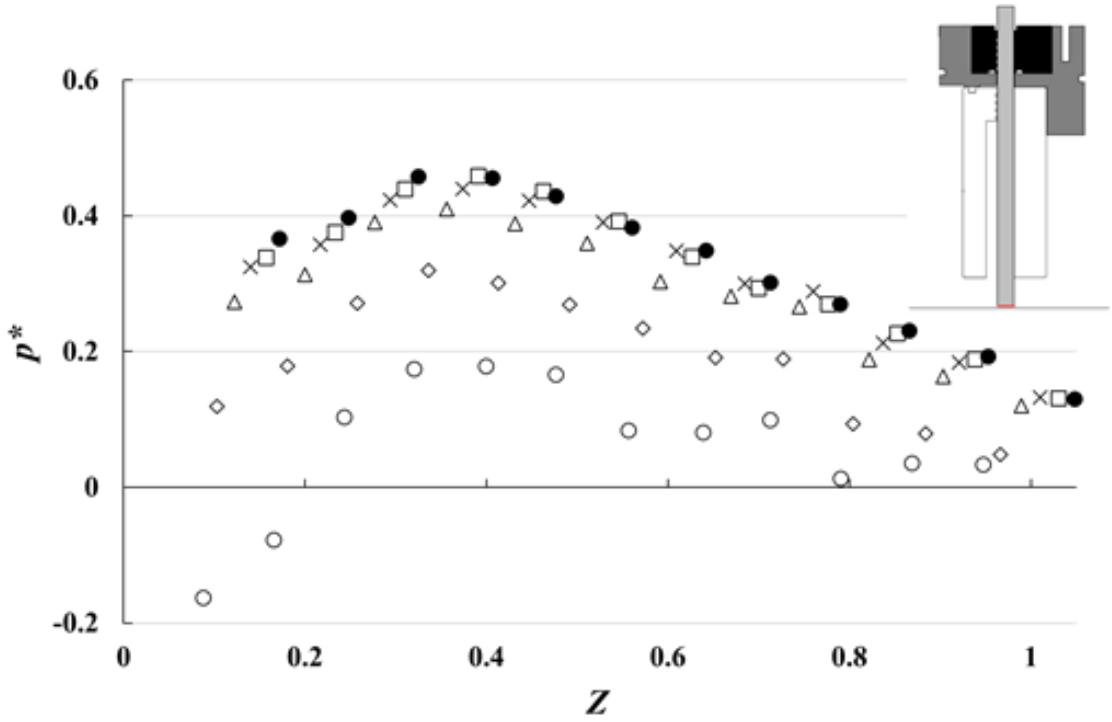

Figure 10: Axial distribution of pressure at the bristle tips, H1, (highlighted) for *c* = 1.9 and over the range of operating conditions described in Table 4.

5.2 Intermediate Clearance Condition, *c* = 1.0

The axial distribution of pressure within the test section was studied for six operating conditions for c = 1.0, as shown in Table 5. Results are shown for positions *H0* and *H1* in Fig. 11 and Fig. 12, respectively. Once again, all data presented in this section is for an atmospheric downstream boundary condition, where p_d = ATM, to study the effect of changing pressure ratio.

For low pressure ratios, the axial distribution of pressure at *H0* (Fig. 11) behaves consistently with that seen for c = 1.9 The presence of the initial, sharp reduction in pressure diminishes with increasing R_p; at R_p = 4.9 the two-stage pressure drop is no longer evident and the axial reduction in pressure on the rotor surface is near-linear from $-0.05 < Z < 1.15$.

Similar behaviour to that for the c = 1.9 case is also noted in Fig. 12, which indicates the effect of increasing R_p and the deflection of the bristle pack.

Convergence in p^* at both *H0* and *H1*, which can be seen in Fig. 11 and Fig. 12 respectively, is evident for $R_p \geq 4.0$; this corresponds to Φ approaching an asymptote, as seen in Fig. 6 for c = 1.0. Figure 12 indicates the presence of a similar low-pressure region, with positive pressure gradients seen for $R_p \leq 2.3$ up to the fourth bristle row. At larger R_p values, the positive pressure gradient does not exist, but the effect of the low-pressure region is still apparent.

Table 5: Operating conditions for each data set at the c = 1.0 clearance condition. For all cases, p_d = ATM.

Test	Δp (bar)	p_u (bar)	R_p
○	0.5	1.5	1.5
◇	1.3	2.3	2.3
△	2.3	3.3	3.3
✕	2.9	3.8	4.0
□	3.3	4.3	4.4
●	3.8	4.7	4.9

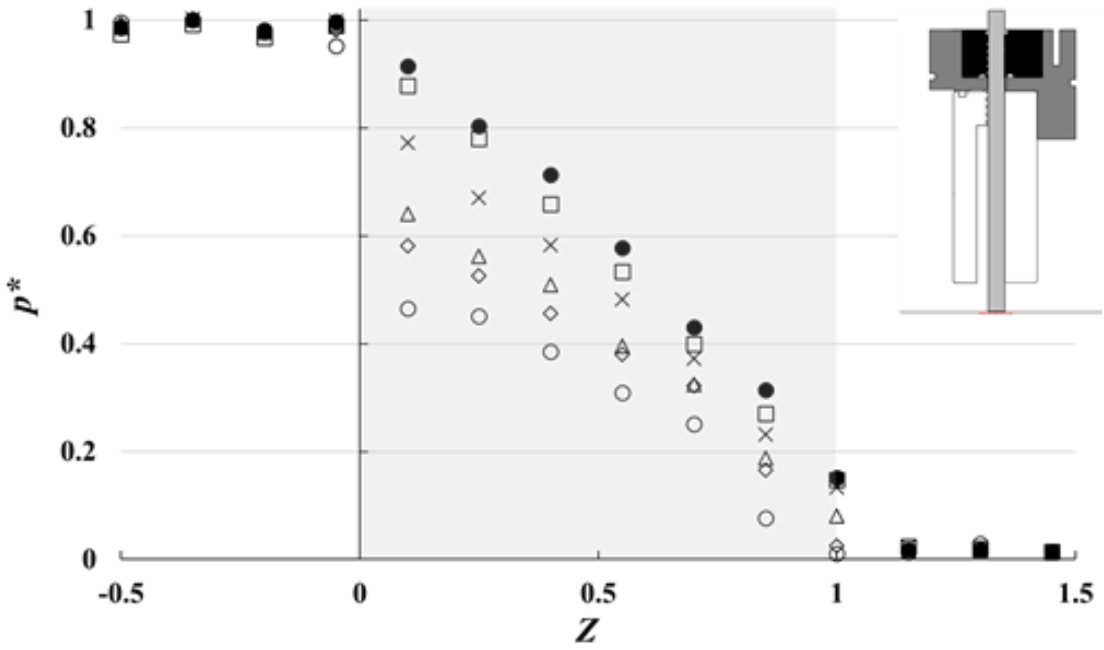

Figure 11: Axial distribution of pressure on the rotor surface, *H0,* (highlighted) for *c* = 1.0 and over the range of operating conditions described in Table 5. The unloaded bristle pack location is indicated by the shaded region.

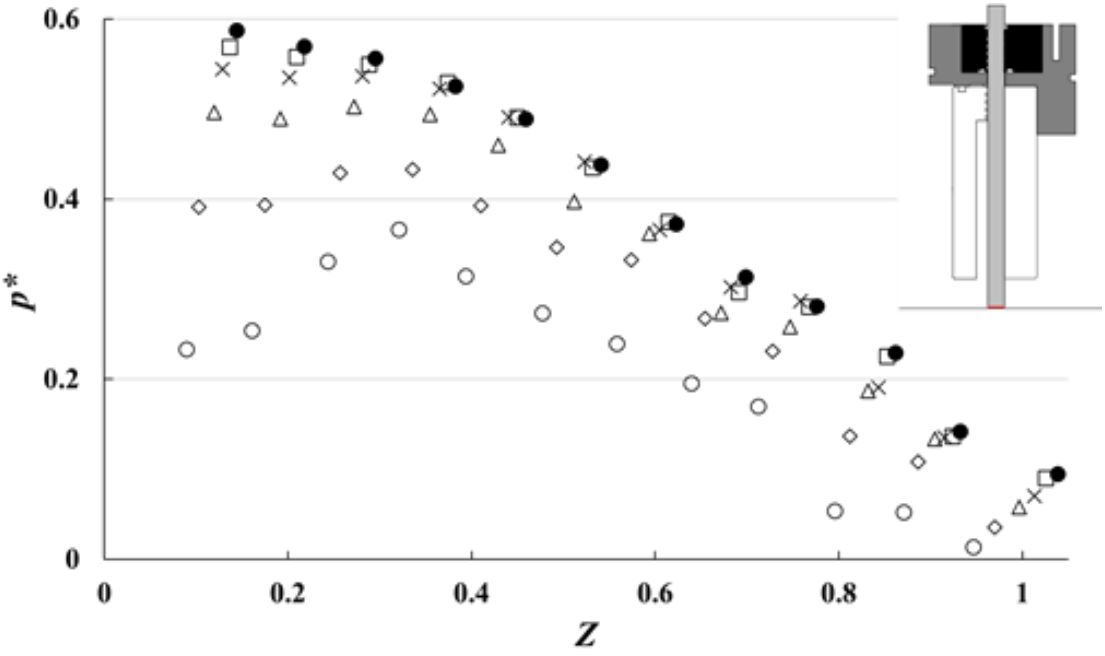

Figure 12: Axial distribution of pressure at the bristle tips, *H1,* (highlighted) for *c* = 1.0 and over the range of operating conditions described in Table 5.

5.3 Line-on-Line (LoL) Condition

The axial distribution of pressure within the test section of the LBS is presented here for the line-on-line condition; the operating conditions are detailed in Table 6. Results are shown for positions *H0* and *H1* in Fig. 13 and Fig. 14 respectively. Although not shown here explicitly, the distributions of pressure for the LoL case indicated that p^* through the bristle pack was principally dependant on Δp, as was the case for Φ shown in Fig. 7. The data presented in this section is for an atmospheric downstream boundary condition, where p_d = ATM. Therefore, the pressure load varies as the upstream pressure, p_u, is increased.

On the rotor surface (Fig. 13), the pressure gradient progressively steepens with axial distance through the bristle pack as the resistance to the flow increases. This behaviour can be explained by the proximity to the back plate which acts to restrict the through-flow area and provides added resistance to the flow. The strong spanwise pressure gradient on the back plate face influences the flow and causes the axial gradient of p^* to become steeper.

The pressure distributions considered in this study demonstrate very similar trends regardless of R_p or Δp at *H0* (Fig. 13) for the LoL case. This is also true at the bristle tips (Fig. 14) for the data sets where $\Delta p \geq 3.0$ bar; this implies that the reduction in bristle pack porosity with further increases in Δp is small. Inspection of Fig. 7 shows that increases in pressure load have a small effect on Φ throughout, with an asymptote reached at $\Delta p \approx 2.0$ bar, and so these similar porosities are expected. This finding is different to results published by Bayley & Long [12] and Chen *et al.* [13] [14] (see Fig. 2), who found differences between data sets for both clearance and interference brush seals, possibly due to the extra stability provided by the deep front plate shroud. Hence

the normalised pressure, p^*, in the test section of the LBS for a LoL configuration is primarily dependent on axial position, Z.

Table 6: Operating conditions for each data set at the line-on-line condition. For all cases, p_d = ATM.

Test	Δp (bar)	p_u (bar)	R_p
○	0.5	1.5	1.5
◇	1.6	2.6	2.6
△	3.0	4.0	4.0
✕	4.1	5.1	5.2
□	5.4	6.4	6.5
●	6.4	7.4	7.6

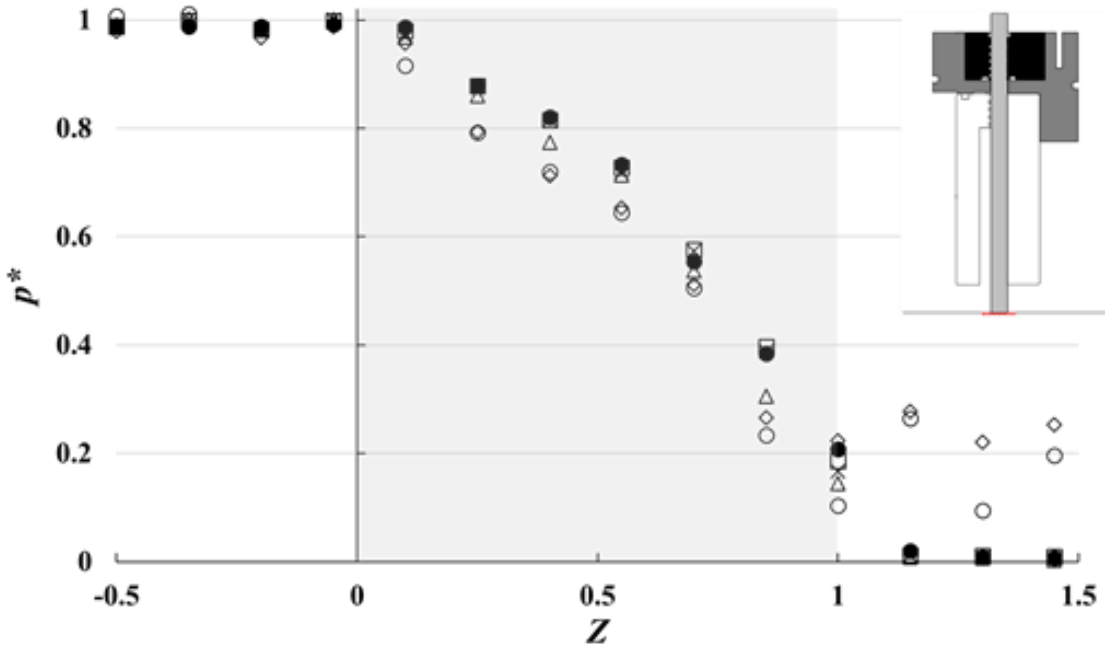

Figure 13: Axial distribution of pressure on the rotor surface, *H0*, (highlighted) for the line-on-line condition and over the range of operating conditions described in Table 6. The unloaded bristle pack location is indicated by the shaded region.

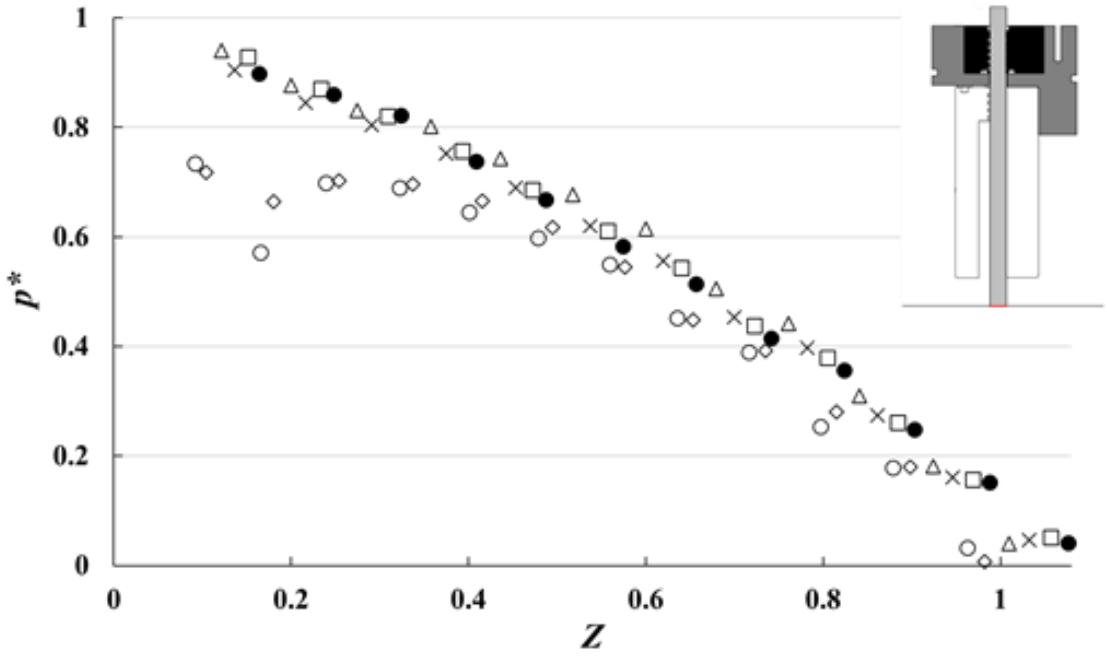

Figure 14: Axial distribution of pressure at the bristle tips, *H1*, (highlighted) for the line-on-line condition and over the range of operating conditions described in Table 6.

5.4 Effect of Clearance on Inter-Bristle Pressure Field

In this sub-section, the pressure distributions are compared directly for the three clearance configurations; comparisons are drawn at three radial locations within the test section: *H0*, *H1* and *H4*, shown in Fig. 15, Fig. 16, and Fig. 17 respectively. Data sets were chosen with consistent operating conditions so that the spanwise clearance was the controlling variable in each case. The experimental conditions are summarised in Table 7.

The impact of the seal clearance on the axial distribution of pressure on the rotor surface is apparent from Fig. 15. The greatest dissimilarity between the three clearances exists from $0 < Z < 0.5$. For the large clearance case (c = 1.9), this region accounts for the majority of the change in p^*. For c = 1.0, less blow-down is required to consistently

close the clearance through-flow area, which is mostly achieved for the Δp = 3.3 bar load shown in Fig. 15, causing a uniform pressure gradient until $p^* \approx 0$. Therefore, the extent of this initial pressure drop is always more pronounced at a given Δp for the larger seal clearance (Fig. 9). For the LoL case, p^* in the $0 < Z < 0.5$ region is larger than for the two clearance cases, as the influence of the seal clearance has been completely removed.

The distributions of axial pressure at the bristle tips for the three clearances, shown in Fig. 16, again indicate a change in brush seal behaviour as c reduces. An inflexion in pressure gradient is present at the fourth bristle row for the two clearance cases which are influenced by a low-pressure region at the leading-edge of the bristle pack. The magnitude and strength of this diminishes as the bristle tips move closer to the rotor surface, both because of increased blow-down at greater pressure loads, as well as reduced clearance. Therefore, a steeper positive pressure gradient exists before the fourth bristle row for the larger clearance condition. With no clearance area for the LoL case, no low-pressure region can form and static pressure in the frontmost bristle rows is much closer to p_u than for the two clearance conditions. Although both c = 1.9 and c = 1.0 demonstrate similar distributions downstream of the inflexion point, the p^* values for the LoL case are larger.

Figures 10, 12, 14 and 16 primarily show data from all three clearances of the axial distributions of pressure at *H1*, but also illustrate the axial tip deflection by accounting for the shift in Z position. Analysis of these figures does not indicate a significant change in bristle deflection, and hence pack compaction, between the clearance and LoL configurations, despite the pressure drop characteristics being markedly different. A focussed investigation on the axial bristle tip deflection can be seen in Appendix A,

which demonstrates that tip deflection for the first and final bristle rows is very similar for each clearance case at a given Δp. The change in form of pressure distribution for the LoL condition from the clearance cases is therefore attributed to the lack of clearance flow, which would otherwise bypass the bristle pack.

From inspection of the axial distributions of pressure at *H0* and *H1* for each clearance case in Fig. 9-14, data for the LoL case is broadly independent of pressure load or ratio in comparison to the clearance cases for the conditions tested. Increasing Δp and R_p results in bristle deflections that cause both blow-down and pack compaction. Isolating the effects of changes in compaction, which determines the pack porosity, through study of the LoL configuration had small effects on Φ and p^* between the considered data sets, as seen in Fig. 7, 13 and 14. However, for the clearance conditions, the magnitude of blow-down as well as compaction changed between the studied data sets, which presented significant differences in Φ and p^*. Therefore, bristle blow-down was more impactful to brush seal performance in this study than pack compaction.

Data for a high-span location (*H4*) measured in the bristle pack and on the back plate face at $Z = 1$, as illustrated in Fig. 5a, is shown in Fig. 17. All three data sets follow a common, near linear trend from the front row of the bristle pack to $Z = 1$ on the back plate face. Here, the static pressure remains significantly larger than p_d, with $p^* \approx 0.4$. A spanwise pressure gradient therefore exists on the back plate surface as the flow passes down the back plate edge towards the fence height region.

Table 7: Operating conditions for each data set presented in the comparison of seal clearance. For all cases, p_d = ATM.

Test	c	Δp (bar)	p_u (bar)	R_p
●	1.9	0.5	1.5	1.5
●	1.0	1.6	2.6	2.6
●	LoL	3.0	4.0	4.0

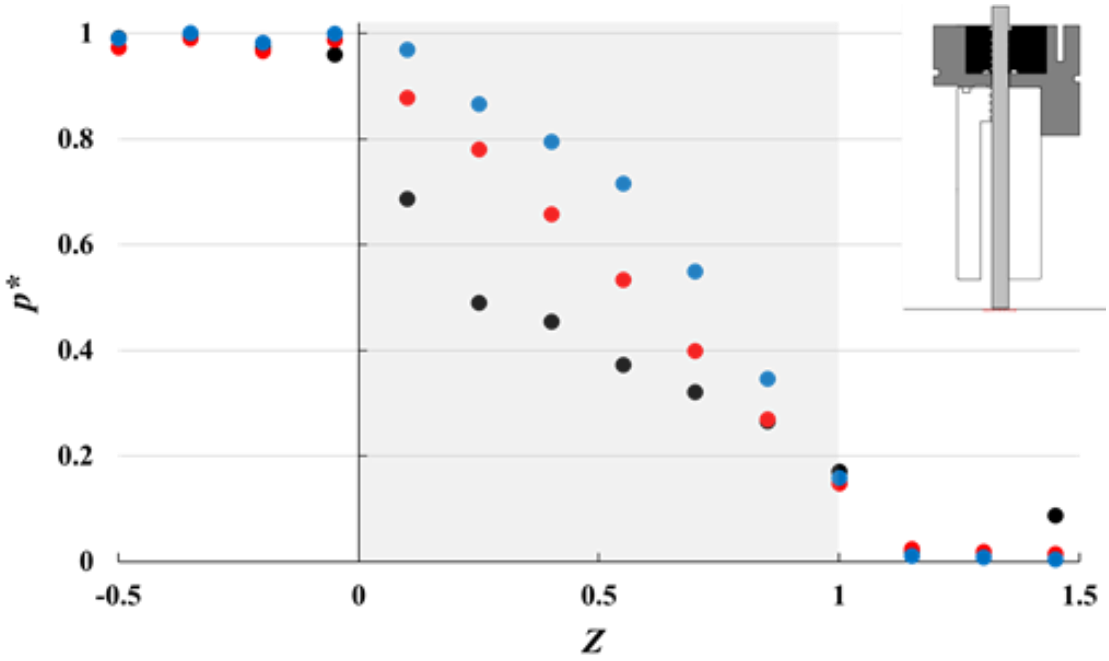

Figure 15: Axial distribution of pressure on the rotor surface, *H0*, (highlighted) for all three clearances at the operating conditions described in Table 7. The unloaded bristle pack location is indicated by the shaded region.

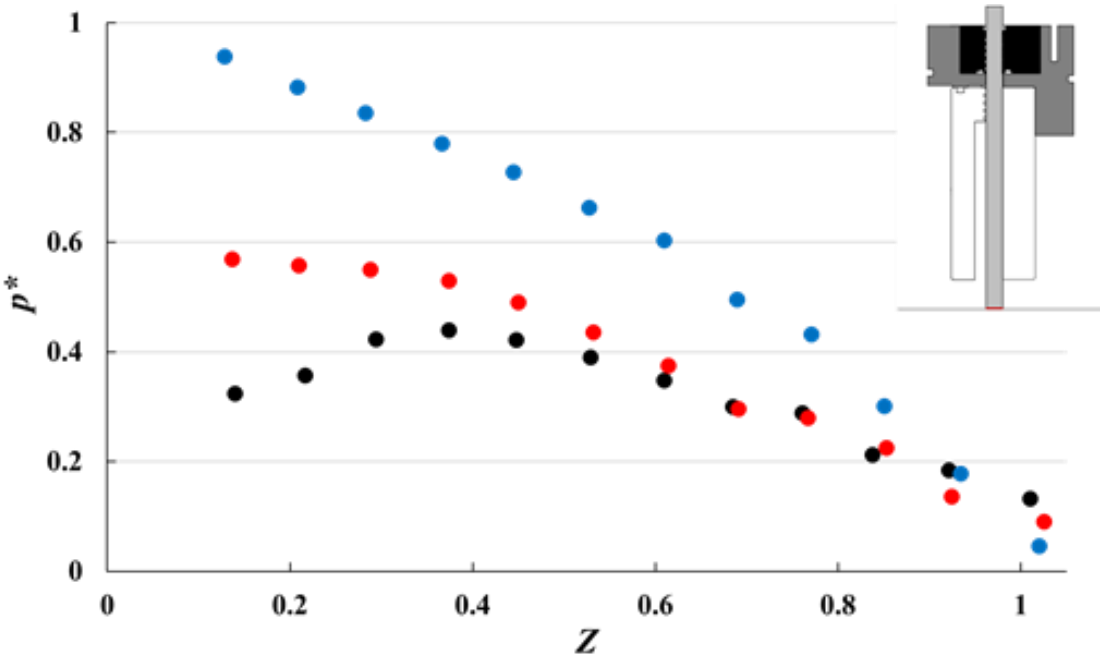

Figure 16: Axial distribution of pressure at the bristle tips, *H1*, (highlighted) for all three clearances at the operating conditions described in Table 7.

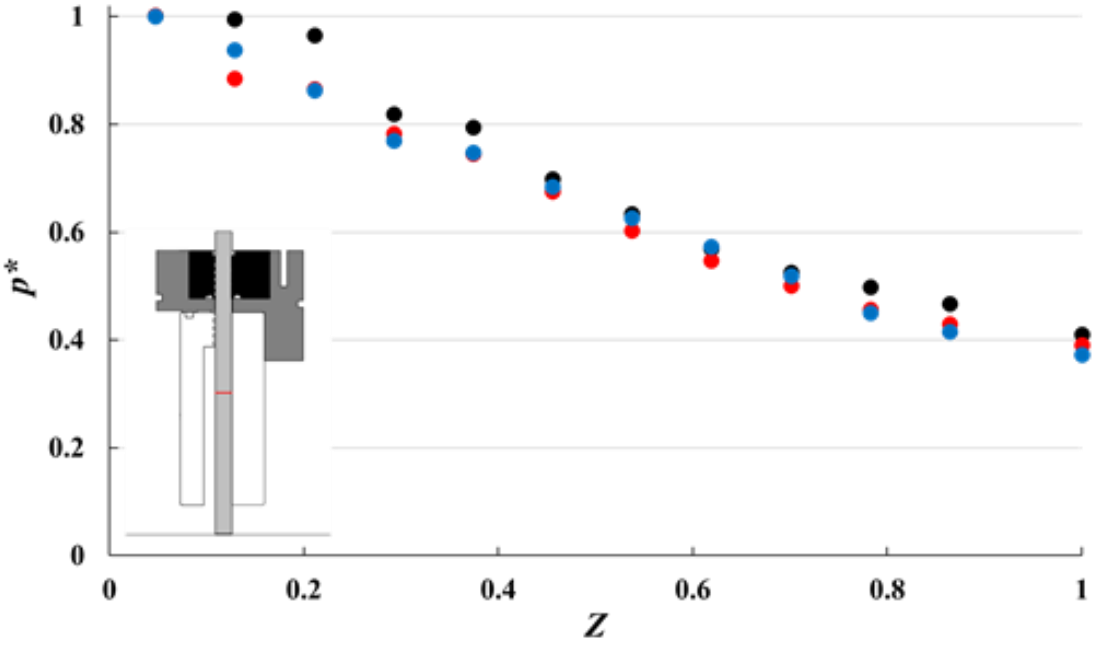

Figure 17: Axial distribution of pressure at the high span position *H4*, (highlighted) including the back plate surface, for all three clearances at the operating conditions described in Table 7.

6 CONCLUSIONS

This paper describes results from a large-scale brush seal testing facility, manufactured to develop an understanding of brush seal fluid dynamic behaviour. The leakage behaviour was characterised in *direct relation* to the inter-bristle pressure field; static pressure data was examined within the bristles, on the back plate, on the rotor surface, as well as at the upstream and downstream boundary conditions across a range of loading conditions. Two spanwise seal clearance cases and a line-on-line configuration were studied.

The governing parameter of brush seal leakage behaviour was found to transition from pressure ratio for a large clearance to pressure load for the line-on-line configuration. In all conditions, an asymptotic value of normalised leakage was reached once the maximum levels of bristle blow-down and pack compaction were achieved. The value of Φ decreased with seal clearance in accordance with enhanced flow resistance.

For both clearance configurations, the distributions of axial pressure on the rotor surface and at the bristle tips converged at pressure differentials corresponding to the asymptotic normalised leakage flow. This was also true for the LoL case for which the dependence of pressure load was smallest and distributions at a given location showed a very similar, continuous pressure drop that is explained by the corresponding small changes in normalised leakage. Such behaviour showed that changes in bristle blow-down had a more significant impact on seal performance than bristle pack compaction in this study.

A two-stage pressure drop was identified on the rotor surface for the two clearances cases due to inconsistent blow-down through the bristle pack. The severity of this

behaviour diminished with increasing pressure differential and reducing clearance. These configurations also experienced a low-pressure region underneath the leading edge of the bristle pack; the impact of this region reduced as the bristle tips moved closer to the rotor surface due to greater blow-down at larger pressure ratios as well as smaller spanwise clearances.

The interrogation of the flow field in this study presents data over an extended range of pressure loadings and clearance conditions with greater accuracy and geometrical similitude than has been previously published, resulting in a more thorough analysis of the fluid dynamic behaviour of brush seals. Therefore, this study can be utilized for the calibration of more accurate porous medium models that will further enhance the application of brush seals in turbomachinery.

DATA ACCESS

Due to confidentiality agreements with research collaborators, supporting data can only be made available to bona fide researchers subject to a nondisclosure agreement. Details of how to request access are available at the University of Bath data archive (http://dx.doi.org/10.15125/BATH-00116).

ACKOWEDLEGEMENTS

This work was supported by the UK Engineering and Physical Sciences Research Council, under the grant number EP/P008232/1. The authors wish to thank Paul Frith, Andrew Langley, Terry Warder and James Cansell for their assistance with the manufacture and assembly of the test rig.

NOMENCLATURE

ATM	atmospheric
c	normalised spanwise clearance (c_m/D)
c_{eff}	effective clearance [mm]
δc_{eff}	error in c_{eff}
c_m	LBS spanwise clearance [mm]
D	bristle tip diameter [mm]
E	bristle material Young's modulus [Pa]
h_f	fence height [mm]
h_{fb}	free bristle height [mm]
L	fence height clearance ($c_m + h_f$) [mm]
LBS	large-scale brush seal
$\dot{m}$	leakage flow rate [kg/s]
p	static pressure [bar]
Δp	pressure load across the LBS ($p_u - p_d$) [bar]
p^*	normalised static pressure
δp^*	error in p^*
p_d	downstream static pressure [bar]
p_u	upstream static pressure [bar]
Q	flow coefficient [$K^{1/2}$ s/m]
R	gas constant [J/kg K]
R_p	pressure ratio across the LBS (p_u/p_d)
SAS	secondary air system
t_{bp}	bristle pack thickness [mm]

T gas flow static temperature [K]

w test section depth [mm]

y spanwise location [mm]

Y normalised spanwise location

z axial location [mm]

z_{fb} axial clearance between front and back plate [mm]

Z normalised axial location

z_1 front plate rear edge to bristle tip axial distance (unloaded) [mm]

z_2 front plate rear edge to bristle tip axial distance (loaded) [mm]

Δz $z_2 - z_1$ [mm]

ρ gas flow density [kg/m^3]

φ bristle pack lay angle [°]

Φ normalised leakage flow rate

$\delta\Phi$ error in Φ

APPENDIX A: BRISTLE DEFLECTION ANALYSIS

The axial deflection of the bristle pack was determined by utilizing the glass window rotor surface described in Section 3.2. Optical access of the test section through the rotor surface gave an uninhibited view of the bristle tips.

A camera was fixed in place to record the bristle pack whilst experimentation was conducted. Figures 18 and 19 show screenshots from the video recorded during a test for which the operating conditions were c = 1.0, Δp = 2.85 bar and p_d = ATM. Figures 18 and 19 show the unloaded and loaded bristle pack, respectively.

The video analysis utilized the software package *ImageJ*, which allows crosshairs to be placed over an image to determine the location of a feature in terms of number of pixels from the top left corner of the image. The procedure is described below, with reference to Fig. 18 and 19:

Step 1:

i. Multiple crosshairs placed along the rear edge of the front plate to determine its exact axial position for each unloaded and loaded case

Step 2:

i. Crosshairs were placed appropriately to measure the width of the bristle tips

ii. Bristle diameters were measured in the first and last rows for both unloaded and loaded conditions, which were compared to ensure that the camera was level during recording

Step 3:

i. Crosshairs were placed on the front of each analysed bristle tip (the hollow bristles that allowed for static pressure measurements at the bristle tips were used for this purpose to eliminate the risk of misidentification)

ii. The distance from the front plate rear edge was calculated from the collected data for both the unloaded (z_1) and loaded (z_2) conditions

iii. The deflection for each bristle row for the specific operating condition was found using Eq. A1

$$\boldsymbol{\Delta z = z_2 - z_1} \qquad \textbf{(A1)}$$

The axial deflection of the bristle tips was calculated for each bristle row for the three clearance conditions over a range of pressure loads. All data presented were

acquired with an atmospheric boundary condition at the outlet, where p_d = ATM. This data was utilised for the distribution of axial pressure analyses presented in Section 5.

The axial deflection of the bristle tips was found to be independent of the seal clearance and governed purely by the pressure load. For clarity, the deflection data for the large clearance case (c = 1.9) at the first and rearmost rows of the bristle pack only is presented in Fig. 20.

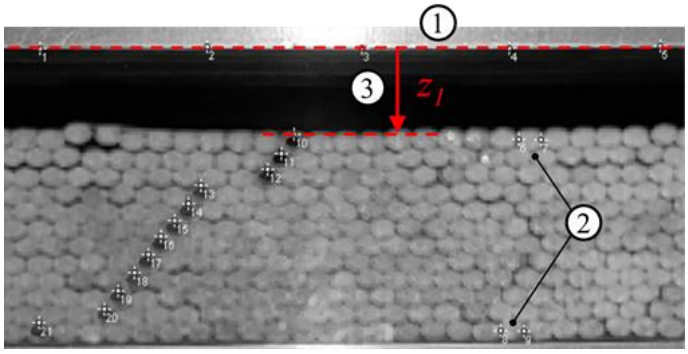

Figure 18: Screenshot of the unloaded bristle pack of the LBS during deflection analysis.

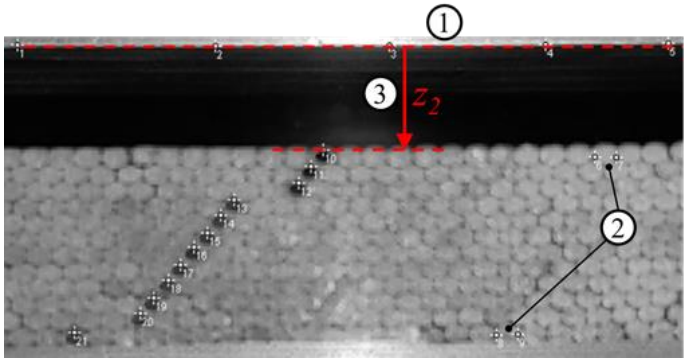

Figure 19: Screenshot of the loaded bristle pack of the LBS during deflection analysis.

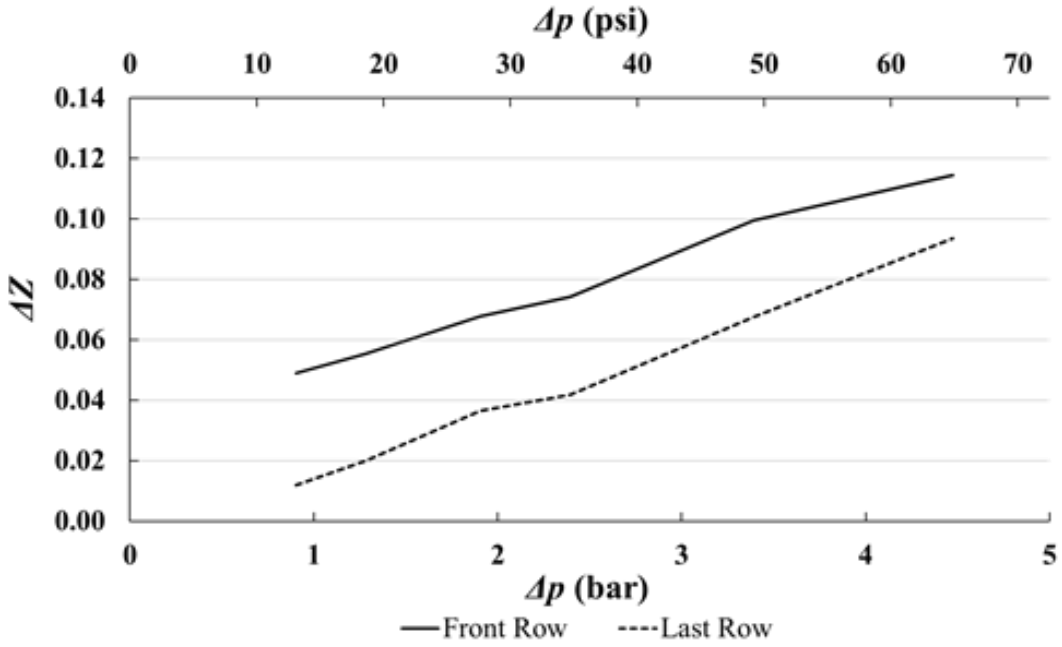

Figure 20: Axial deflection of the bristles in the front and last rows of the bristle pack for the large clearance condition (*c* = 1.9) over a range of operating conditions.

APPENDIX B: UNCERTAINTY ANALYSIS

This uncertainty analysis has been carried out according to the methodology of Coleman & Steele [21] and Moffat [22]. Table 8 gives an estimate of the measurement uncertainties of p^* and Φ for the large clearance condition (c = 1.9), which was taken for the data point at which p_u = 2.87 bar, p_d = ATM and $\dot{m}$ = 0.36 kg/s.

Table 9 gives the precision and specification of the instrumentation.

The normalised pressure (p^*), leakage flow rate ($\dot{m}$), and effective clearance (c_{eff}) is defined as following:

$$p^* = \frac{p - p_d}{p_u - p_d} \quad \textbf{(A2)}$$

$$\Phi = \frac{\dot{m}\sqrt{RT}}{p_u L^2} \quad \textbf{(A3)}$$

$$c_{eff} = \frac{\dot{m}\sqrt{T}}{w p_u Q} \quad \textbf{(A4)}$$

When the geometric uncertainties are ignored, the uncertainties can be calculated as follows:

$$\left(\frac{\delta p^*}{p^*}\right)^2 = \left(\frac{\delta p}{p-p_d}\right)^2 \left(\frac{\delta p}{p}\right)^2 + \left(\frac{p_u(p_d-p)}{(p-p_d)(p_u-p_d)}\right)^2 \left(\frac{\delta p_u}{p_u}\right)^2 + \left(\frac{p_d}{p_d-p}\right)^2 \left(\frac{\delta p_d}{p_d}\right)^2 \quad \textbf{(A5)}$$

$$\left(\frac{\delta \Phi}{\Phi}\right)^2 = \left(\frac{\delta \dot{m}}{\dot{m}}\right)^2 + \left(\frac{\delta T}{T}\right)^2 + \left(\frac{\delta p_u}{p_u}\right)^2 \quad \textbf{(A6)}$$

$$\left(\frac{\delta c_{eff}}{c_{eff}}\right)^2 = \left(\frac{\delta \dot{m}}{\dot{m}}\right)^2 + \left(\frac{\delta T}{T}\right)^2 + \left(\frac{\delta p_u}{p_u}\right)^2 + \left(\frac{\delta p_d}{p_d}\right)^2 \quad \textbf{(A7)}$$

When applied to the axial distribution of pressure results from this study, such as that on the rotor surface for the large clearance condition (shown in Fig. 21 which includes the magnitude of error in p^* for each data point), the relationship between R_p and experimental uncertainty is apparent. For smaller pressure ratios, the results are subject to a larger error because of the smaller p_u, p, and $\dot{m}$ values recorded. It was found that the majority of the experimental error was associated with the measurement of p_d as this was very small and unchanged in all cases; therefore, the magnitude of error converged at large pressure ratios.

Table 8: Estimated measurement uncertainty.

Dimension	**Uncertainty**
$\delta p^*/p^*$	2.6%
$\delta \Phi/\Phi$	1.3%
$\delta c_{eff}/c_{eff}$	2.9%

Table 9: Precision and specification of the instrumentation.

X_i	δX_i	Scale Range (units)	Instrument
p_u, p_d, p	±0.25% FSS	0 - 10 bar	HMA Series Amplified Pressure Sensors
$\dot{m}$	±0.25% FSS	0 - 0.3506 kg/s	Bronkhorst F-106CI
T	±0.5 K	3 – 1530 K	K-Type Thermocouple
Δz	±0.0336 mm	0 – 1.32 mm	Video Analysis

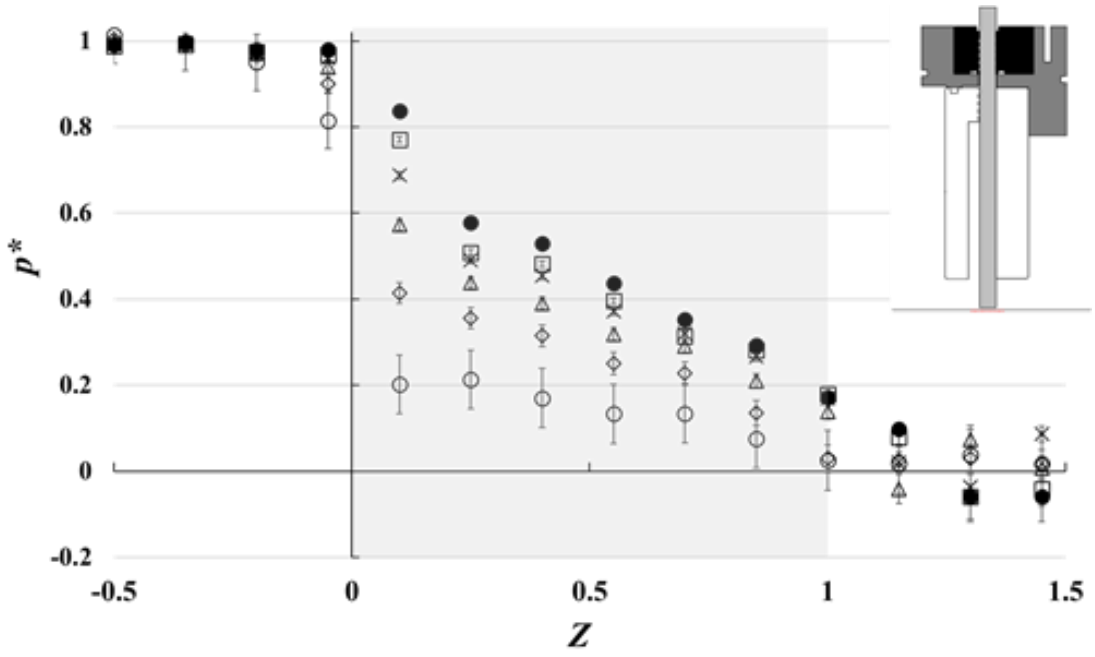

Figure 21: Axial distribution of pressure on the rotor surface, *H0*, for *c* = 1.9 and over the range of operating conditions described in Table 4. The magnitude of error in *p for each data point in included.**

References

[1] R. E. Chupp, R. C. Hendricks, S. B. Lattime and B. M. Steinetz, "Sealing in Turbomachinery," *J Propulsion and Power,* vol. 22, no. 2, pp. 313-349, 2006.

[2] F. E. Aslan-Zada, . V. A. Mammadov and F. Dohnal, "Brush Seals and Labyrinth Seals in Gas Turbine Applications," *J Power and Energy,* vol. 227, no. 2, pp. 216-230, 2012.

[3] S. Dinc, M. Demiroglu, N. Turnquist, J. Mortzheim, G. Goetze, J. Maupin, J. Hopkins, C. Wolfe and M. Florin, "Fundamental Design Issues of Brush Seals for Industrial Applications," *Journal of Turbomachinery,* vol. 124, no. 2, pp. 293-300, 2002.

[4] J. G. Ferguson, "Brushes as High Performance Gas Turbine Seals," *Proceedings of the ASME Turbo Expo,* vol. 182, 1988.

[5] C. Carey, O. Inderwildi and D. King, "Sealing Technologies – Signed , Sealed and Delivering Emissions Savings," *Aviation and the Environment,* pp. 44-48, 2009.

[6] R. C. Hendricks, T. A. Griffin, T. R. Kline, K. R. Csavina, A. Pancholi and D. Sood, "Relative Performance Comparison Between Baseline Labyrinth and Dual-Brush Compressor Discharge Seals in a T-700 Engine Test," *39th Interntional Gas Turbine and Aerospace Congress and Exposition,* 1994.

[7] G. Franceschini, T. V. Jones and D. R. H. Gillespie, "Improved Understanding of Blow-Down in Filament Seals," *Journal of Turbomachinery,* vol. 132, no. 4, 2010.

[8] M. J. Pekris, G. Franceschini and D. Gillespie, “An Investigation of Flow, Mechanical, and Thermal Performance of Conventional and Pressure-Balanced Brush Seals,” *Journal of Engineering for Gas Turbines and Power,* vol. 136, no. 6, 2014.

[9] J. A. Schlumberger, M. P. Proctor and R. C. Hendricks, “Eccentricity Effects on Leakage of a Brush Seal at Low Speeds,” *1991 Winter Annual Meeting of the American Society of Mechanical Engineers,* 1991.

[10] J. A. Carlile, R. C. Hendricks and D. A. Yoder, “Brush Seal Leakage Performance with Gaseous Working Fluids at Static and Low Rotor Speed Conditions,” *ASME 1992 International Gas Turbine and Aeroengine Congress and Exposition, GT 1992,* vol. 115, pp. 397-403, 1992.

[11] T. Kirk, A. Bowsher, P. Crudgington and R. Chupp, “Aspects of Brush Seal Design,” *51st AIAA/SAE/ASEE Joint Propulsion Conference,* 2015.

[12] F. J. Bayley and C. A. Long, “A Combined Experimental and Theoretical Study of Flow and Pressure Distributions in a Brush Seal,” *J. Eng. Gas Turbines Power,* vol. 115, no. 2, pp. 404-410, 1993.

[13] L. Chen, “Numerical and Experimental Modelling of Brush Seals,” University of Oxford, Oxford, 1998.

[14] L. H. Chen, P. E. Wood, T. V. Jones and J. W. Chew, “Detailed Experimental Studies of Flow in Large Scale Brush Seal Model and a Comparison with CFD Predictions,” *Proceedings of the ASME Turbo Expo,* vol. 122, pp. 672-679, 2000.

[15] M. J. Braun, R. C. Hendricks and V. Canacci, “Flow Visualization in a Simulated Brush Seal,” *Proceedings of the ASME Turbo Expo,* vol. 5, 1990.

[16] Y. Doğu, “Investigation of Brush Seal Flow Characteristics Using Bulk Porous Medium Approach,” *Journal of Engineering for Gas Turbines and Power,* vol. 127, no. 1, pp. 136-144, 2005.

[17] P. F. Crudgington, “Brush Seal Performance Evaluation,” in *34th AIAA/ASME/SAE/ASEE Joint Propulsion Conference and Exhibit*, 1998.

[18] P. Crudgington, A. Bowsher, D. Lloyd and J. Walia, “Bristle Angle Effects on Brush Seal Contact Pressures,” in *45th AIAA/ASME/SAE/ASEE Joint Propulsion Conference and Exhibit,* 2009.

[19] E. Pedraza-Valle, “Development of a Rotating Test Facility for the Experimental Characterisation of Turbomachinery Shaft Seals,” Univeristy of Bath PhD Thesis, 2020.

[20] Y. Doğu, M. C. Sertçakan, A. S. Bahar, A. Pişkin, E. Arıcan and M. Kocagül, “CFD Investigation of Brush Seal Leakage Performance Depending on Geometric Dimensions and Operating Conditions,” *J. Eng. Gas Turbines Power,* vol. 138, no. 3, March 2016.

[21] H. W. Coleman and W. G. Steele, “Engineering Application of Experimental Uncertainty Analysis,” *AIAA,* vol. 33, no. 10, pp. 1888-1896, 1995.

[22] R. J. Moffat, “Describing the Uncertainties in Experimental Results,” *Experimental Thermal and Fluid Science,* vol. 1, no. 1, pp. 3-17, 1988.